

Synergistic effect of multiple reactive oxygen species via orbital-reconstructed tungsten for indoor acetaldehyde photocatalytic oxidation

Zixiang Xu ¹, Wenqiang Qu ¹, Qiuying Yi, Danhong Cheng ^{*}, Dengsong Zhang ^{*}

International Joint Laboratory of Catalytic Chemistry, Innovation Institute of Carbon Neutrality, Department of Chemistry, College of Sciences, Shanghai University, Shanghai 200444, China

ARTICLE INFO

Key words:

Environmental catalysis
Photocatalysis
Gaseous acetaldehyde purification
Tungsten oxide

ABSTRACT

The visible-light photocatalytic elimination of indoor acetaldehyde, a prevalent volatile organic compound, remains a significant challenge. Despite that tungsten oxide photocatalysts emerge as promising catalysts for acetaldehyde degradation indoors, their energy band structure often limits the removal performance by favoring the generation of a single reactive oxygen species. Herein, we showed a 5d orbital-reconstructed tungsten-based photocatalyst induced by g-C₃N₄ support, notably enhancing acetaldehyde elimination under visible light. Experimental and theoretical findings demonstrated that the 5d orbital reconstruction induced an upward shift in the unoccupied orbital of tungsten site, thereby facilitating the generation of superoxide radicals. Furthermore, hydroxy radicals can efficiently convert acetaldehyde into acetic acid, followed by the rapid elimination of acetic acid intermediates. This synergistic effect among multiple oxygen species significantly amplifies acetaldehyde elimination indoors, and offers new insights into the interactions between reactive species and pollutants in photocatalytic environmental applications.

1. Introduction

The prevailing living scene for the contemporary individuals primarily occur indoors [1], underscoring the imperative significance of ensuring indoor air safety for the protection of human health. Acetaldehyde, the prototypical indoor volatile organic compound (VOCs) [2–4], emerges as deleterious to human well-being [5,6]. In homes and workplaces, second-hand smoke, paint and treated wood are the main source of acetaldehyde pollution [7]. To eliminate the indoor VOCs with dilute concentration, various technologies have been employed [8,9], among which the photocatalytic oxidation method stands as an ideal technique for indoor air purification, owing to its environmentally friendly and efficacious properties [10–12]. During the photocatalytic oxidation process, the reactive species can be generated by the photocatalyst under the light illumination, which will in turn attack the pollutant molecules [13,14]. Titanium dioxide, well-known as the most ubiquitous photocatalyst for pollutant mitigation [15,16], exhibits a limitation in its responsiveness solely to ultraviolet (UV) light [17,18]. However, the indoor illumination condition predominantly comprises

visible light components in the form of lamps [19,20]. Therefore, developing new-type photocatalysts attuned to indoor lighting conditions emerges as pivotal in the quest to eliminate indoor acetaldehyde.

Among the numerous reported photocatalysts, tungsten-oxide-based catalysts are considered as one of the most promising options for indoor acetaldehyde degradation [21–23]. The properties of narrow bandgap ($E_g \approx 2.8$ eV) and appropriate valence-band (VB, 3.0 V versus NHE) potential for tungsten oxide (WO_3), endow it with excellent visible-light responsibility and hydroxyl-radicals generation capability, respectively [24]. However, the low conduction-band (CB, 0.4 V versus NHE) potential of WO_3 -based catalysts makes the handicap of superoxide radical generation [25]. Notably, the notable challenge lies in the intermediate's activation by the single species of hydroxyl radicals, especially for the acetic acid species, which limits the degradation performance of WO_3 -based catalysts under indoor conditions [26,27]. To enhance the degradation efficiency of WO_3 photocatalysts, various strategies have been developed [28,29]. Zhou et al. successfully synthesized the Ag doped Z-scheme Bi_2WO_6/WO_3 heterojunction, which not only increased the absorption of visible light, but also improved the

* Corresponding authors.

E-mail addresses: cdh@shu.edu.cn (D. Cheng), dszhang@shu.edu.cn (D. Zhang).

¹ These authors contribute equally to this work.

separation efficiency of photogenerated carriers, achieving the efficient removal of gaseous volatile organic compounds [30]. Choi et al. presented a WO_3 photocatalyst coated with the hydroscopic periodic acid, where the in-situ formed water layer selectively concentrates the acetaldehyde, dramatically enhancing the photocatalytic removal efficiency [25]. Yet, these methods primarily enhance the light absorption or carrier migration process, without effectively altering the redox potential of photocatalysts, thus cannot overcome the limitations between hydroxyl radicals and reaction intermediates on WO_3 -based photocatalysts. Consequently, tailoring the interactions between reaction intermediates and reactive oxygen species is imperative to enhance the performance of tungsten-based photocatalysts in eliminating indoor acetaldehyde.

Herein, we designed a 5d-orbital-reconstructed WO_3 photocatalyst induced by carbon nitride ($\text{g-C}_3\text{N}_4$). The upward shift of W 5d orbital enhanced the reduction potential for the WO_3 , thereby facilitating the generation of superoxide species. Experimental findings revealed the acetaldehyde degradation pathway on the 5d-orbital-reconstructed photocatalyst, where multiple oxygen radicals were involved in tandem. The acetaldehyde molecules were converted into acetic acid in the function of hydroxyl radicals, followed by being eliminated through a novel pathway with superoxide radicals, which remarkably enhanced the degradation efficiency of acetaldehyde under indoor condition. This synergistic interplay among multiple oxygen species overcomes the limitations observed in tungsten-based catalysts for acetaldehyde elimination within indoor environments, and offers valuable insights for indoor air purification.

2. Experimental section

2.1. Chemicals

Urea (NH_2CONH_2 , GENERAL-REAGENT) and ammonium metatungstate hydrate ($(\text{NH}_4)_6\text{H}_2\text{W}_{12}\text{O}_{40} \cdot \text{XH}_2\text{O}$, Shanghai Aladdin Biochemical Technology) were commercial and used without any further purification.

2.2. Catalysts preparation

2.2.1. Preparation of CN catalyst

The CN sample was synthesized according to the report [31]. Typically, 10 g of urea was deposited in a crucible, followed by being heated at 550 °C for 4 h with a heating rate of 2.3 °C/min. The as-prepared light yellow powder was then heated again at 500 °C for 5 h with a heating rate of 5 °C/min. The resulting sample was then obtained and named as CN.

2.2.2. Preparation of WCN catalyst

0.2 g of CN sample and 0.1 g of ammonium metatungstate hydrate were added to 40 ml of deionized water, following by being agitation for 5 h with a heating rate of 5 °C/min. The suspension was then dried through rotary evaporation. The obtained power was then calculated to 500 °C and kept for 3 h with a heating rate of 5 °C/min. After cooling down to ambient temperature, the resulting powder was named WCN.

2.2.3. Preparation of WO catalyst

For comparison, the pristine WO_3 catalyst was synthesized. Specifically, 0.5 g of ammonium metatungstate hydrate was heated to 500 °C and kept for 3 h with a heating rate of 5 °C/min. The as-prepared sample was noted as WO.

2.3. Photocatalytic performance evaluation

The photocatalytic degradation performance evaluation was carried on a continuous flow reactor, as we reported before [13]. Typically, 40 mg of photocatalyst was uniformly deposited in a 275 ml home-made

reactor. Simulated contaminated air (50 ppm of acetaldehyde, 21% of O_2 , 79% of N_2 , and 6000 ppm of H_2O) with the flow rate of 40 ml/min was then fed into the reactor for 1 h under dark condition. After the adsorption-desorption equilibrium of acetaldehyde, the light (300 W xenon lamp with a 420 nm cut-off filter, PLS-XE300, Perfectlight, Beijing) was introduced to initiate the degradation reaction. The light intensity was measured by using an optical power meter (PL-MW2000, Perfectlight, Beijing), and the results showed that the light intensity on the catalyst surface was about 0.18 W/cm². The concentration of acetaldehyde was monitored by the gas chromatograph (GC-2014 C, Shimadzu) with a flame ionization detector, and the concentration of CO_2 was detected by a photoacoustic spectrometer (GASERA ONE, Beijing Duke Technology Co., Ltd.).

2.4. Characterization

X-ray diffraction was tested on a Bruker D8 diffractometer with a Cu K α radiation. The scanning electron microscopy (SEM, JSM-7500 F) and high-resolution transmission electron microscopy (HR-TEM, JEM-2100 F) were performed to characterize the catalysts' morphology. X-ray photoelectron spectroscopy (XPS) and valance band X-ray photoelectron spectroscopy (Vb-XPS) were examined in an X-ray photoelectron spectrometer (Kratos Axis DLD, Japan). UV-vis diffuse reflectance spectra (UV-vis DRS) were obtained on UV-vis-NIR spectrophotometer (Carry 5000, Aglient, USA) with BaSO_4 as a reference. Photoluminescence spectra (PL) and time-resolved photoluminescence (TRPL) were measured by a spectrophotometer (Edinburgh FS1000). Electrochemical impedance spectroscopy (EIS) curves were obtained on CHI 760E electrochemistry workstation. Electron paramagnetic resonance (EPR, EMX-8/2.7, Bruker) spectra were performed to detect the reactive oxygen species with 5,5-dimethyl-1-pyrroline N-oxide (DMPO). *In-situ* DRIFTS for photocatalytic degradation of acetaldehyde were conducted on a FT-IR spectrometer (Nicolet is50, Thermo Scientific, USA).

3. Results and discussion

3.1. Synthesis and characterization of WCN sample

After impregnating the ammonium metatungstate onto the $\text{g-C}_3\text{N}_4$ (CN) nanosheet and going through a calcination, the targeted 5d-orbital-reconstructed WO_3 -based photocatalyst was prepared, as illustrated in Fig. 1. The as-prepared sample was denoted as WCN. The powder X-ray diffraction (XRD) was then used to characterize sample's crystal structure, as displayed in Fig. 2a. It was noteworthy that both WCN and WO samples exhibited the similar diffraction peaks (JCPD No. 72-0677) [32], but a lower peak intensity was revealed on WCN sample, which was consistent with the Raman analysis (Fig. S1). Notably, the specific peak for CN sample was originated from the (002) facet of $\text{g-C}_3\text{N}_4$ nanosheet, while such peak was absent on WCN sample [33]. During the preparation of WCN sample, the WO_3 nanoparticles were in-situ grown between the $\text{g-C}_3\text{N}_4$ nanolayers, which resulted in a huge change in the interplanar spacing for $\text{g-C}_3\text{N}_4$, subsequently responsible for the peak disappearance.

Furthermore, the microscopic morphology was observed by scanning electron microscopy (SEM, Figs. S2 and S3), transmission electron microscopy (TEM, Fig. S4) and high-resolution transmission electron microscopy (HRTEM, Fig. 2b). Notably, the disordered lattice was observed on $\text{g-C}_3\text{N}_4$, which resulted from the thin layer structure of the support. Simultaneously, the crystal plane spacing of WO_3 on WCN sample was revealed to be 0.381 nm, corresponding to the (002) facet of WO_3 [34]. Therefore, the WCN photocatalyst was successfully synthesized, fundamentally characterized as the $\text{g-C}_3\text{N}_4$ supported WO_3 photocatalyst.

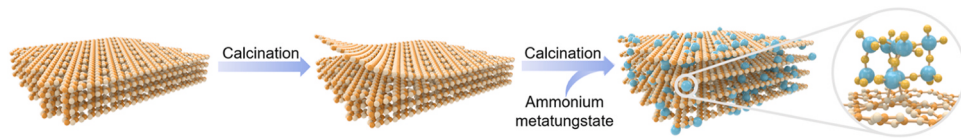


Fig. 1. Schematic of the preparation for WCN photocatalysts.

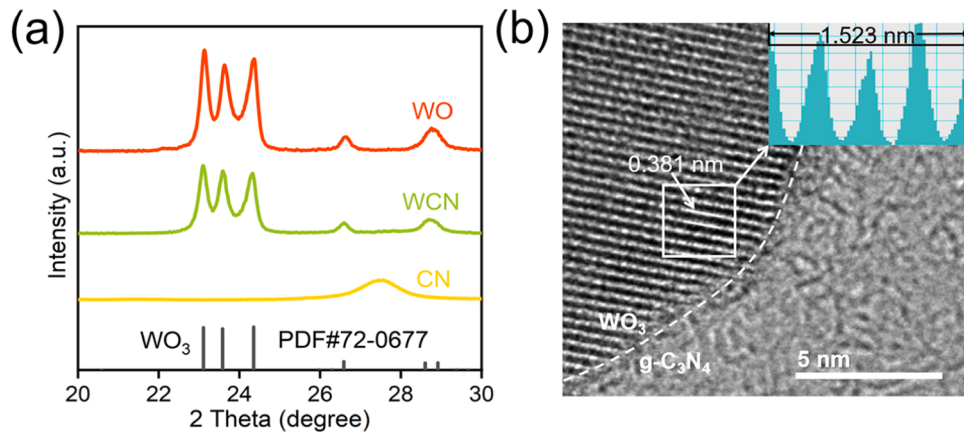


Fig. 2. (a) XRD patterns for WO, WCN and CN photocatalysts. (b) HRTEM image for WCN photocatalysts (Inset: the corresponding crystal plane spacing image).

3.2. Electronic structure characterization

In order to get an insight into the electronic structure of WCN

photocatalyst, X-ray photoelectron spectroscopy (XPS) was employed [35,36]. The W 4f high-resolution XPS spectra was displayed in Fig. 3a, and the results indicated that the peak of WCN sample (35.3 and

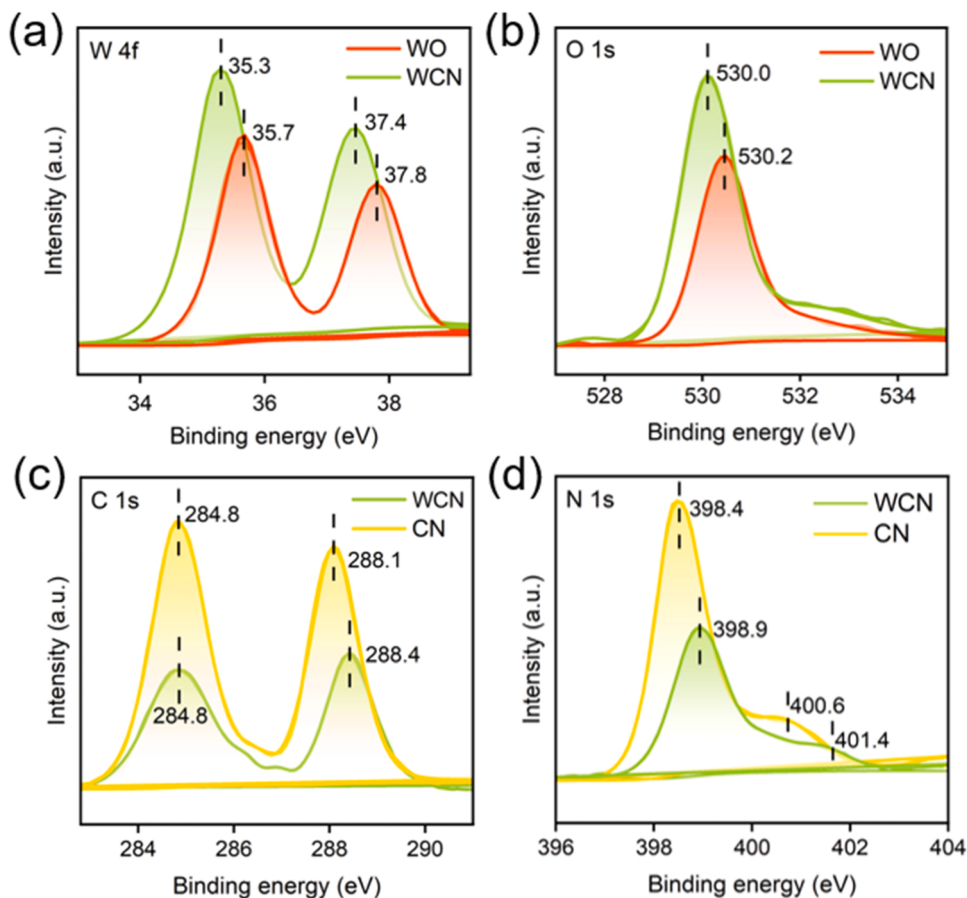


Fig. 3. High-resolution XPS spectra of (a) W 4f and (b) O 1s for WO and WCN photocatalysts. High-resolution XPS spectra of (c) C 1s and (d) N 1s for WCN and CN photocatalysts.

37.4 eV) shifted towards lower binding energy compared to the WO counterpart (35.7 and 37.8 eV). This shift indicated a lower valence state of W site in WCN sample, signifying an increasing number occupied electron. Additionally, the O 1 s peak of WCN sample (530.0 eV) shifted to a lower binding energy than WO sample, suggesting more valence electron of oxygen in WCN sample. The C 1 s and N 1 s high-resolution XPS spectra were shown in Figs. 3c and 3d, respectively. The C 1 s peak of WCN sample (288.4 eV) moved towards higher binding energy relative to the CN sample (288.1 eV), while the N 1 s peak of WCN (398.9 eV) also shifted towards higher binding energy compared to the CN sample (398.4 eV). Thereby, in comparison with the WO sample, the W and O sites of WCN gained the electrons. Conversely, in contrast to the CN sample, the C and N sites of WCN lose electrons. This observation indicated that the g-C₃N₄ support can effectively transfer electrons to WO₃ in the WCN sample.

To further understand the electron transfer within WCN sample, density functional theory (DFT) was employed. Differential charge density and Bader charge analysis were conducted on the optimized WCN model, as depicted in Fig. 4a. An evident charge transfer occurred on the interface between WO₃ and g-C₃N₄, and the transfer was actually mainly taking place between the N site (g-C₃N₄) and the W site (WO₃). Bader charge analysis further revealed that each N site transferred 0.16 electrons to the W site, which was identical with the experimental results. Previously, it was reported that the electron back-donation enable the charge transfer from N 2p to the d orbital of metal site, which can result in the observed electron change of W site [37].

Furthermore, the electronic structures of the W and N sites were studied through the projected density of state (PDOS) [37]. For the electronic structure of W, as illustrated in Fig. 4b. The asymmetric spins (up and down) were exhibited on WO sample. However, the electronic energy level of W 5d underwent a remarkable change after the electron acquisition, in which the up and down spins became symmetrical, indicating that the W 5d electronic energy level was reconstructed triggered by the interface formation between WO₃ and g-C₃N₄. Additionally, the unoccupied orbital of W site moved towards higher energy level (away from the Fermi level), which would leave a significant impact on the reduction potential for the photocatalyst's conduction band. For the electronic structure of N site, as shown in Fig. 4c. The energy level did not change significantly, which suggested that the electron transfer just changed the valence electron number, but has limited impact on the energy level position for N site.

Hence, the g-C₃N₄ effectively transferred electrons to WO₃ within WCN photocatalyst. More importantly, the W 5d electronic energy level underwent the reconstruction under the electron transfer from N to W site, with its unoccupied W 5d orbital moving towards higher energy level, which will leave a remarkable effect on the reduction potential of the photocatalysts, and a profound affection on the photocatalyst's efficacy in degrading acetaldehyde.

3.3. Photocatalytic degradation performance for indoor acetaldehyde

To evaluate the acetaldehyde elimination performance of the 5d-orbital-reconstructed WCN photocatalyst, the simulated air containing 50 ppm of acetaldehyde was introduced into a continuous flow reactor, and the tests were carried under visible light (> 420 nm). Before initiating the reaction, the photocatalysts were treated under dark condition for 40 min. When the gas components reached stable, the visible light was then introduced, and the corresponding concentration during the acetaldehyde degradation process was displayed in Figs. 5a and S5. The CN catalyst exhibited a negligible efficiency in acetaldehyde degradation under visible light, and the WO catalyst showed a moderate removal efficiency. Notably, the WCN photocatalyst displayed a significantly enhanced acetaldehyde elimination performance compared to the other samples, signifying the superiority of the 5d-orbital-reconstructed WCN photocatalyst in purifying acetaldehyde under indoor conditions. Furthermore, the CO₂ concentration during the degradation process was also detected, as shown in Fig. 5b. The enhanced CO₂ generation for WCN photocatalyst revealed its superior capability in detoxifying acetaldehyde pollutant compared to the WO and CN samples. Notably, compared with traditional TiO₂ photocatalyst, WCN photocatalyst also showed significantly better performance (Fig. S6).

Under continuous flow gas containing acetaldehyde, the WCN photocatalyst was also tested prolonging reaction time, as illustrated in Fig. 5c. The WCN maintained an efficient degradation performance within 600 min, and the XRD spectra (Fig. S7) between the photocatalysts before and after the test were nearly consistent, showing a robust stability for sustained catalytic requirements in degradation acetaldehyde. The performance of catalysts was tested in the batch reactor, and WCN photocatalyst exhibited the consistent result to that in flow reactor.

Hence, the 5d-orbital-reconstructed WCN photocatalyst displayed a remarkably enhanced performance in acetaldehyde degradation under indoor conditions. The acetaldehyde degradation experiments were also performed in a batch reactor (Fig. S8), and the results were identical to the continuous flow reactor, further indicating that the exceptional performance WCN photocatalyst in acetaldehyde degradation within indoor condition.

3.4. Photoelectric properties characterization

To elucidate the origin of the enhanced acetaldehyde degradation performance for the WCN photocatalyst, the photoelectric properties were initially discussed. The light absorption capability was investigated via ultraviolet-visible diffuse reflectance spectroscopy (UV-Vis DRS) [38,39], as shown in Fig. 6a. Notably, the absorption threshold within low-wavelength range of WCN sample decreased compared to WO sample, which attributed to the widened bandgap of WO₃ within the 5d orbital-reconstructed WCN photocatalyst [40]. The corresponding tauc-plot curves (Fig. S8) further corroborated such deduction, where

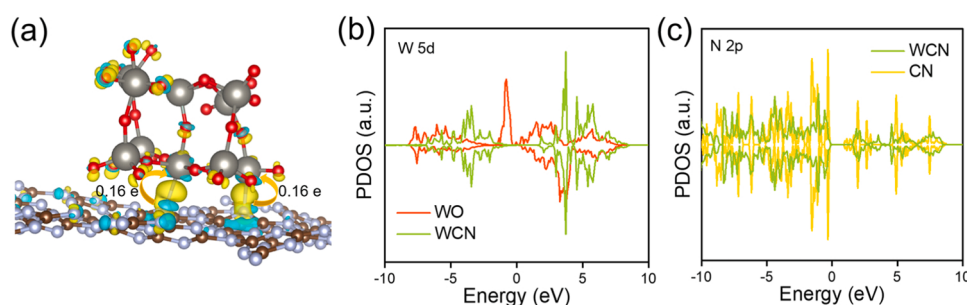


Fig. 4. (a) Differential charge density between the WO₃ and g-C₃N₄ within WCN photocatalyst. The cyan and yellow colors represent the decrease and increase of electron density, respectively. The dark brown, white, red and gray atoms represent the carbon, nitrogen, oxygen and tungsten atoms, respectively. (b) PDOS profile of W 5d orbital on WO and WCN photocatalysts. (c) PDOS profile of N 2p orbital on WCN and CN photocatalysts.

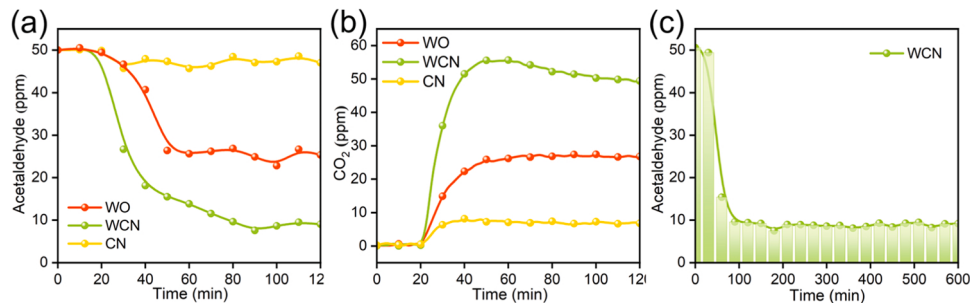


Fig. 5. Plots of concentration of (a) acetaldehyde and (b) CO₂ versus time over WO, WCN and CN photocatalysts. (c) Plots of concentration of acetaldehyde with long-time test over WCN photocatalyst. Reaction conditions: 50 ppm of acetaldehyde, 6000 ppm of H₂O balanced with air, 40 mg of photocatalysts under the flow rate of 40 ml/min, and irradiated under visible light with light intensity of 0.1 W/cm².

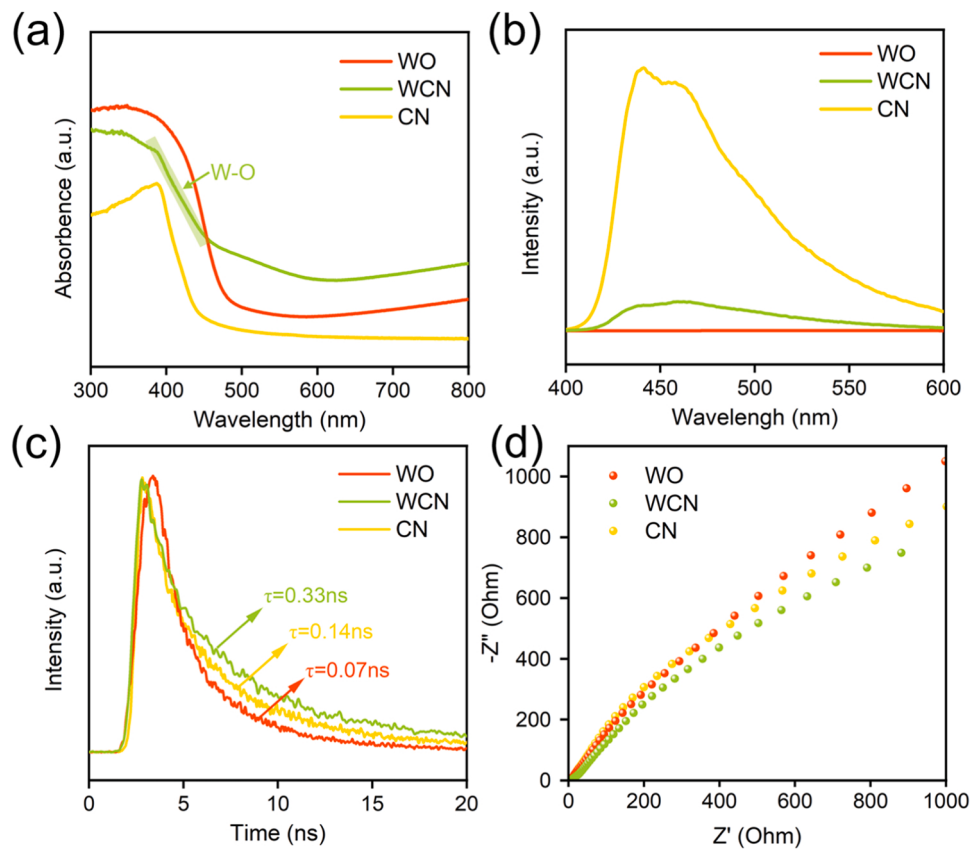


Fig. 6. (a) UV-vis DRS, (b) PL, (c)TRPL and (d) EIS curves for WO, WCN and CN photocatalysts.

the bandgap of WCN was measured at 2.72 eV but that in WO was 2.61 eV. Based on the preceding results, it can be known that the conduction band (CB) of tungsten (W) in the WCN shifts to a higher energy level, which might be the pivotal reason of the widened bandgap, and has been further proved by the Mott-schottky plots (Fig. S10).

The photogenerated carrier separation process was then studied, and the photoluminescence (PL) spectroscopy was conducted, as demonstrated in Fig. 6b. Due to the degradation experiments were performed under visible light, the excitation wavelength was then set at 420 nm. In comparison with CN sample, the PL intensity of WCN photocatalyst significantly reduced, indicating the separation of photogenerated charge carriers can be promoted within WCN [41]. Besides, the WO₃ did not exhibit a discernible PL signal, which might be attributed to either the limited number of photogenerated carriers under visible light within the WO₃ catalyst.

The time-resolved photoluminescence (TRPL) spectroscopy was then

utilized to further investigate the lifetime of photogenerated carrier [42, 43], as depicted in Fig. 6c. a prolonged carrier lifetime was observed on WCN photocatalyst (0.33 ns), showing 2.4 and 4.7 times to that of CN (0.14 ns) and WO (0.07 ns), respectively. Moreover, electrochemical impedance spectroscopy (EIS) was employed to assess the carrier migration capabilities of the samples [44,45]. The diameter of the semicircle in the Nyquist diagram serves as an indicator of the charge transfer resistance, as depicted in Fig. 6d. The results demonstrated that the WCN sample shows the lowest resistance, aligning with the observations in TRPL. Due to the 5d orbital reconstruction, the conduction band (CB) position shifted upward, while the valence band (VB) potential moved downward, leading to the expansion of bandgap. Notably, the upward CB potential would endow the capability for superoxide radicals (See in next section), which would further consume the photogenerated electrons, thus promoting the carrier separation process. Consequently, the orbital reconstruction in WCN induced an expansion

in the bandgap of WO_3 , concurrently promoting the separation of photogenerated carriers.

3.5. Reaction mechanism for photocatalytic degradation of acetaldehyde

The reactive oxygen species (ROS) played a pivotal role in the VOCs degradation process, and can engage in the oxidation of carbonaceous intermediates [46,47]. To understand the ROS on WCN photocatalyst during the acetaldehyde degradation, the generated superoxide radicals ($\cdot\text{O}_2^-$) and hydroxyl radicals ($\cdot\text{OH}$) under visible light irradiation for 10 min were detected by electron paramagnetic resonance (EPR) spectra [48,49]. For the $\cdot\text{O}_2^-$ species, as shown in Fig. 7a, the WCN photocatalyst exhibited an enhanced DMPO- $\cdot\text{O}_2^-$ signal in comparison to the WO and CN samples. This enhancement was resulted from the fact that the conduction band energy level shifted upward due to the 5d orbital reconstruction within WCN photocatalyst, further increasing the reduction potential of photocatalyst and enhancing the generation of $\cdot\text{O}_2^-$ species. In parallel, the WCN catalyst exhibits a substantially amplified signal for DMPO- $\cdot\text{OH}$ compared to WO and CN counterparts, as shown in Fig. 7b. Consequently, the WCN photocatalyst showed a pronounced efficiency in production in both $\cdot\text{O}_2^-$ and $\cdot\text{OH}$ species. Besides, it was noteworthy that the WO catalyst exhibited the least capability for $\cdot\text{O}_2^-$ generation and a moderate capacity for $\cdot\text{OH}$, attributed to its low conduction band position [50,51].

To elucidate the effect of different ROS generation behavior on acetaldehyde degradation pathway, the in-situ diffused reflectance infrared Fourier transform spectroscopy (in-situ DRIFTS) was employed to monitor the surface intermediates during acetaldehyde degradation. All samples were pretreated with $20 \text{ ml}\cdot\text{min}^{-1}$ pure air at 80°C for 30 min to remove surface impurities. After cooling to room temperature, the simulated air containing 50 ppm of acetaldehyde was introduced for 40 min, and the surface signal was then collected as the background line. Under the light illumination for 80 min, the signals were recorded every 10 min to analyze the surface intermediates during acetaldehyde degradation. As shown in Fig. 8a, as the reaction going on, some peaks gradually emerged and accumulated on WCN photocatalyst. The peaks can be specifically attributed to the methoxyformic acid (1170 cm^{-1}) [52] formic acid (1222 cm^{-1}) [53], and acetic acid ($1305\text{--}1444 \text{ cm}^{-1}$) [54] species. However, only the acetic acid species were observed on the WO catalyst, with the absence of other intermediates, as shown in Fig. 8b. Considering the different ROS generation behavior, it can be inferred that the $\cdot\text{OH}$ can effectively convert acetaldehyde into acetic acid. However, the subsequent oxidation of acetic acid molecules appeared to be a relatively challenging process. Notably, on the WCN photocatalyst, the $\cdot\text{O}_2^-$ species played a pivotal role in facilitating the further conversion of acetic acid, thereby open up a new degradation

pathway.

Therefore, the reconstruction of 5d orbitals in WCN photocatalyst induced an upward shift on conduction band, thereby enhancing the reduction potential and promoting the generation of $\cdot\text{O}_2^-$. The presence of the $\cdot\text{O}_2^-$ species promoted the oxidation of formic acid intermediates, following the reaction pathway illustrated in Fig. 9, specifically: Acetaldehyde - Acetic acid - Methoxyformic acid - Formic acid - CO_2 . Concurrently, the increased concentration of $\cdot\text{OH}$ species on WCN photocatalyst also sped up the oxidation process of acetaldehyde. Consequently, multiple ROS species synergistically interacted with the acetaldehyde and the intermediates, promoting the degradation of acetaldehyde under indoor conditions.

4. Conclusion

The catalytic abatement of acetaldehyde presents a significant challenge under visible light. As one of the most promising catalysts for indoor acetaldehyde elimination, the tungsten oxide catalyst suffers from significant challenge, due to that their band structure often facilitates the generation of only a single reactive oxygen species. Herein, we tailored a 5d orbital reconstructed WO_3 -based catalyst, where the upward shift of the conduction band facilitated the generation of superoxide species. Experimental findings elucidate an acetaldehyde degradation pathway on the 5d orbital-reconstructed photocatalyst, involving the sequential participation of multiple oxygen radicals. Acetaldehyde molecules undergo conversion into acetic acid through the influence of hydroxyl radicals, subsequently being eliminated via a novel pathway involving superoxide radicals. This synergistic interplay among multiple oxygen species significantly enhances the efficiency of acetaldehyde elimination within indoor environments, and offers valuable insights for indoor air purification.

CRediT authorship contribution statement

Zhang Densong: Writing – review & editing, Visualization, Validation, Resources, Project administration, Investigation, Funding acquisition, Formal analysis, Data curation, Conceptualization. **Yi Qiuying:** Investigation, Formal analysis, Data curation. **Cheng Dan-hong:** Investigation, Formal analysis, Data curation. **Xu Zixiang:** Writing – original draft, Investigation, Formal analysis, Data curation. **Qu Wenqiang:** Investigation, Formal analysis, Data curation.

Declaration of Competing Interest

All authors declare that there are no conflicts of interest, financial or otherwise in this work; and there are no other relationships or activities

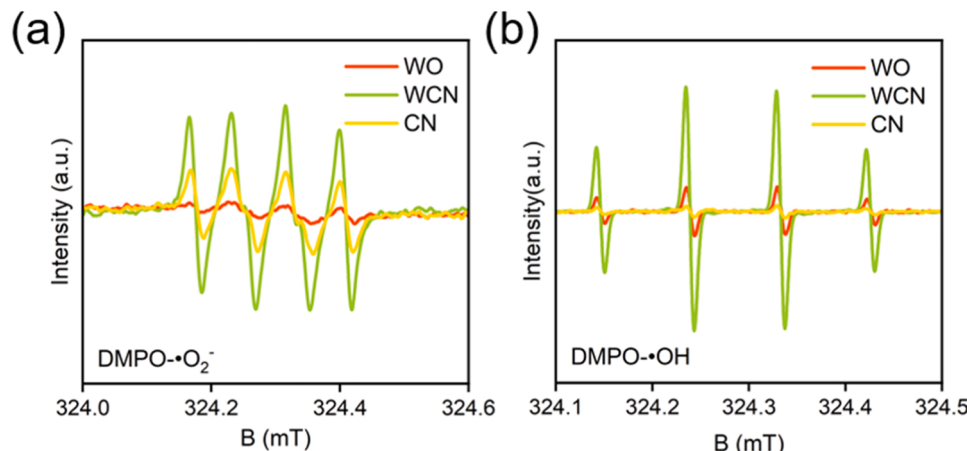


Fig. 7. EPR spectra of (a) DMPO- $\cdot\text{O}_2^-$ and (b) DMPO- $\cdot\text{OH}$ under visible-light irradiation for 10 min on WO, WCN and CN photocatalysts.

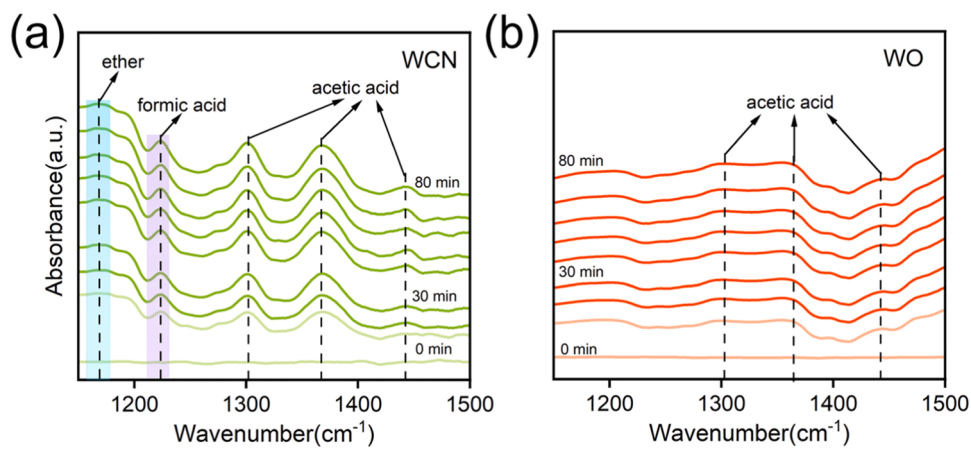


Fig. 8. *In-situ* DRIFTS spectra of acetaldehyde degradation between 1150 and 1500 cm^{-1} over (a) WCN and (b) WO photocatalysts. Reaction conditions: The photocatalysts were treated with the air containing 50 ppm of acetaldehyde for 40 min at 30 °C, and then illuminated by visible light for 80 min.

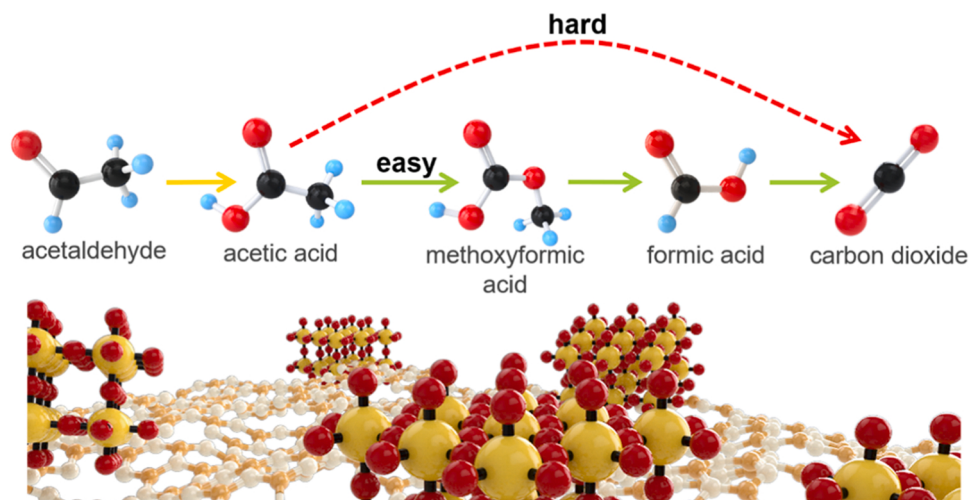


Fig. 9. Schematic illustration for different pathways of photocatalytic gas acetaldehyde degradation.

that can appear to have influenced the submitted work.

Data availability

Data will be made available on request.

Acknowledgements

We acknowledge the support of the National Natural Science Foundation of China (22125604).

Appendix A. Supporting information

Supplementary data associated with this article can be found in the online version at [doi:10.1016/j.apcatb.2024.123763](https://doi.org/10.1016/j.apcatb.2024.123763).

References

- [1] M. Abidi, A.A. Assadi, A. Bouzaza, A. Hajjaji, B. Bessais, S. Rtimi, Photocatalytic indoor/outdoor air treatment and bacterial inactivation on $\text{Cu}_x\text{O}/\text{TiO}_2$ prepared by HiPIMS on polyester cloth under low intensity visible light, *Appl. Catal. B* 259 (2019) 118074, <https://doi.org/10.1016/j.apcatb.2019.118074>.
- [2] C. He, J. Cheng, X. Zhang, M. Douthwaite, S. Pattisson, Z. Hao, Recent advances in the catalytic oxidation of volatile organic compounds: a review based on pollutant sorts and sources, *Chem. Rev.* 119 (2019) 4471–4568, <https://doi.org/10.1021/acscchemrev.8b00408>.
- [3] G. McFiggans, T.F. Mentel, Jr Wildt, I. Pullinen, S. Kang, E. Kleist, S. Schmitt, M. Springer, R. Tillmann, C. Wu, D. Zhao, M. Hallquist, C. Faxon, M. Le Breton, As. M. Hallquist, D. Simpson, R. Bergström, M.E. Jenkin, M. Ehn, J.A. Thornton, M. R. Alfarra, T.J. Bannan, C.J. Percival, M. Priestley, D. Topping, A. Kiendler-Scharr, Secondary organic aerosol reduced by mixture of atmospheric vapours, *Nature* 565 (2019) 587–593, <https://doi.org/10.1038/s41586-018-0871-y>.
- [4] P. Hu, R. Wang, Z. Gao, S. Jiang, Z. Zhao, H. Ji, Z. Zhao, Improved interface compatibility of hollow $\text{H-Zr}_{0.1}\text{Ti}_{0.9}\text{O}_2$ with $\text{UiO}-66-\text{NH}_2$ via Zr-Ti bidirectional penetration to boost visible photocatalytic activity for acetaldehyde degradation under high humidity, *Appl. Catal. B* 296 (2021) 120371, <https://doi.org/10.1016/j.apcatb.2021.120371>.
- [5] A.C. Lewis, The changing face of urban air pollution, *Science* 359 (2018) 744–745, <https://doi.org/10.1126/science.aar4925>.
- [6] J. Li, W. Cui, P. Chen, X. Dong, Y. Chu, J. Sheng, Y. Zhang, Z. Wang, F. Dong, Unraveling the mechanism of binary channel reactions in photocatalytic formaldehyde decomposition for promoted mineralization, *Appl. Catal. B* 260 (2020) 118130, <https://doi.org/10.1016/j.apcatb.2019.118130>.
- [7] R. Nabizadeh, A. Sorooshian, A.N. Baghani, Q. Ashournejad, On the nature of airborne aldehydes in a middle eastern megacity: Tehran, Iran, *Sustain. Cities Soc.* 53 (2020) 101895. (<https://doi.org/10.1016/j.scs.2019.101895>).
- [8] L.-H. Xie, X.-M. Liu, T. He, J.-R. Li, Metal-organic frameworks for the capture of trace aromatic volatile organic compounds, *Chem* 4 (2018) 1911–1927, <https://doi.org/10.1016/j.chempr.2018.05.017>.
- [9] W. Cho, D. Lee, G. Choi, J. Kim, A.E. Kojo, C. Park, Supramolecular engineering of amorphous porous polymers for rapid adsorption of micropollutants and solar-powered volatile organic compounds management, *Adv. Mater.* 34 (2022) 2206982, <https://doi.org/10.1002/adma.202206982>.
- [10] J. Qin, Y. Pei, Y. Zheng, D. Ye, Y. Hu, Fe-MOF derivative photocatalyst with advanced oxygen reduction capacity for indoor pollutants removal, *Appl. Catal. B* 325 (2023) 122346, <https://doi.org/10.1016/j.apcatb.2022.122346>.
- [11] P. Wu, S. Dai, G. Chen, S. Zhao, Z. Xu, M. Fu, P. Chen, Q. Chen, X. Jin, Y. Qiu, S. Yang, D. Ye, Interfacial effects in hierarchically porous $\alpha\text{-MnO}_2/\text{Mn}_3\text{O}_4$

heterostructures promote photocatalytic oxidation activity, *Appl. Catal. B* 268 (2020) 118418, <https://doi.org/10.1016/j.apcatb.2019.118418>.

[12] H. Zhang, S. Sui, X. Zheng, R. Cao, P. Zhang, One-pot synthesis of atomically dispersed Pt on MnO₂ for efficient catalytic decomposition of toluene at low temperatures, *Appl. Catal. B* 257 (2019) 117878, <https://doi.org/10.1016/j.apcatb.2019.117878>.

[13] W. Qu, P. Wang, X. Chen, D. Zhang, Immunizing sulfate-mediated deactivation over TiO₂ photocatalysts for gaseous benzene purification via self-adaptive deoxygenation of sulfate radicals, *Appl. Catal. B* 321 (2023) 122036, <https://doi.org/10.1016/j.apcatb.2022.122036>.

[14] L. Yan, Q. Wang, W. Qu, T. Yan, H. Li, P. Wang, D. Zhang, Tuning Ti^{δ+}-Vo-Pt^{δ+} interfaces over Pt/TiO₂ catalysts for efficient photocatalytic oxidation of toluene, *Chem. Eng. J.* 431 (2022) 134209, <https://doi.org/10.1016/j.cej.2021.134209>.

[15] C. Liang, C. Li, Y. Zhu, X. Du, C. Yao, Y. Ma, J. Zhao, Recent advances of photocatalytic degradation for BTEX: materials, operation, and mechanism, *Chem. Eng. J.* 455 (2023) 140461, <https://doi.org/10.1016/j.cej.2022.140461>.

[16] Q. Guo, C. Zhou, Z. Ma, X. Yang, Fundamentals of TiO₂ photocatalysis: concepts, mechanisms, and challenges, *Adv. Mater.* 31 (2019) 1901997, <https://doi.org/10.1002/adma.201901997>.

[17] F. He, U. Muliaina, S. Weon, W. Choi, Substrate-specific mineralization and deactivation behaviors of TiO₂ as an air-cleaning photocatalyst, *Appl. Catal. B* 275 (2020) 119145, <https://doi.org/10.1016/j.apcatb.2020.119145>.

[18] Y. Wang, Y. Zhang, X. Zhu, Y. Liu, Z. Wu, Fluorine-induced oxygen vacancies on TiO₂ nanosheets for photocatalytic indoor VOCs degradation, *Appl. Catal. B* 316 (2022) 121610, <https://doi.org/10.1016/j.apcatb.2022.121610>.

[19] A. Galenda, F. Visentin, R. Gerbasi, M. Favaro, A. Bernardi, N. El Habra, Evaluation of self-cleaning photocatalytic paints: are they effective under actual indoor lighting systems? *Appl. Catal. B* 232 (2018) 194–204, <https://doi.org/10.1016/j.apcatb.2018.03.052>.

[20] P. Pichat, A brief survey of the practicality of using photocatalysis to purify the ambient air (indoors or outdoors) or air effluents, *Appl. Catal. B* 245 (2019) 770–776, <https://doi.org/10.1016/j.apcatb.2018.12.027>.

[21] J. Yu, F. Dappozzo, J. Martín-Gomez, J. Hidalgo-Carrillo, A. Marinas, P. Vernoux, A. Caravaca, C. Guillard, Glyceraldehyde production by photocatalytic oxidation of glycerol on WO₃-based materials, *Appl. Catal. B* 299 (2021) 120616, <https://doi.org/10.1016/j.apcatb.2021.120616>.

[22] H.A. Vignolo-González, A. Gouder, S. Laha, V. Duppel, S. Carretero-Palacios, A. Jiménez-Solano, T. Oshima, P. Schützendübe, B.V. Lotsch, Morphology matters: 0D/2D WO₃ nanoparticle-ruthenium oxide nanosheet composites for enhanced photocatalytic oxygen evolution reaction rates, *Adv. Energy Mater.* 13 (2022) 2203315, <https://doi.org/10.1002/aenm.202203315>.

[23] D. Zeng, H. Wang, X. Zhu, H. Cao, W. Wang, Y. Zhang, J. Wang, L. Zhang, W. Wang, Photocatalytic conversion of CO₂ to acetic acid by CuPt/WO₃: chloride enhanced C-C coupling mechanism, *Appl. Catal. B* 323 (2023) 122177, <https://doi.org/10.1016/j.apcatb.2022.122177>.

[24] S. Weon, F. He, W. Choi, Status and challenges in photocatalytic nanotechnology for cleaning air polluted with volatile organic compounds: visible light utilization and catalyst deactivation, *Environ. Sci. Nano* 6 (2019) 3185–3214, <https://doi.org/10.1039/c9en00891h>.

[25] F. He, S. Weon, W. Jeon, M.W. Chung, W. Choi, Self-wetting triphase photocatalysis for effective and selective removal of hydrophilic volatile organic compounds in air, *Nat. Commun.* 12 (2021) 6259, <https://doi.org/10.1038/s41467-021-26541-z>.

[26] H. Irie, S. Miura, K. Kamiya, K. Hashimoto, Efficient visible light-sensitive photocatalysts: grafting Cu(II) ions onto TiO₂ and WO₃ photocatalysts, *Chem. Phys. Lett.* 457 (2008) 202–205, <https://doi.org/10.1016/j.cplett.2008.04.006>.

[27] G. Loget, C. Mériaudec, V. Dorcet, B. Fabre, A. Vacher, S. Fryars, S. Ababou-Girard, Tailoring the photoelectrochemistry of catalytic metal-insulator-semiconductor (MIS) photoanodes by a dissolution method, *Nat. Commun.* 10 (2019) 3522, <https://doi.org/10.1038/s41467-019-11432-1>.

[28] C.T.K. Nguyen, N. Quang Tran, S. Seo, H. Hwang, S. Oh, J. Yu, J. Lee, T. Anh Le, J. Hwang, M. Kim, H. Lee, Highly efficient nanostructured metal-decorated hybrid semiconductors for solar conversion of CO₂ with almost complete CO selectivity, *Mater. Today* 35 (2020) 25–33, <https://doi.org/10.1016/j.mattod.2019.11.005>.

[29] R. Shen, G. Liang, L. Hao, P. Zhang, X. Li, *In situ* synthesis of chemically bonded 2D/2D covalent organic frameworks/O-vacancy WO₃ Z-scheme heterostructure for photocatalytic overall water splitting, *Adv. Mater.* 35 (2023) 2303649, <https://doi.org/10.1002/adma.202303649>.

[30] H. Zhou, Z. Wen, J. Liu, J. Ke, X. Duan, S. Wang, Z-scheme plasmonic Ag decorated WO₃/Bi₂WO₆ hybrids for enhanced photocatalytic abatement of chlorinated-VOCs under solar light irradiation, *Appl. Catal. B* 242 (2019) 76–84, <https://doi.org/10.1016/j.apcatb.2018.09.090>.

[31] X. Hai, Y. Zheng, Q. Yu, N. Guo, S. Xi, X. Zhao, S. Mitchell, X. Luo, V. Tulus, M. Wang, X. Sheng, L. Ren, X. Long, J. Li, P. He, H. Lin, Y. Cui, X. Peng, J. Shi, J. Wu, C. Zhang, R. Zou, G. Guillén-Gosálbez, J. Pérez-Ramírez, M.J. Koh, Y. Zhu, J. Li, J. Lu, Gemini-atom catalysis for cross-coupling, *Nature* 622 (2023) 754–760, <https://doi.org/10.1038/s41586-023-06529-z>.

[32] C. Fábrega, S. Murcia-López, D. Monllor-Satoca, J.D. Prades, M.D. Hernández-Alonso, G. Penelas, J.R. Morante, T. Andreu, Efficient WO₃ photoanodes fabricated by pulsed laser deposition for photoelectrochemical water splitting with high faradaic efficiency, *Appl. Catal. B* 189 (2016) 133–140, <https://doi.org/10.1016/j.apcatb.2016.02.047>.

[33] F. He, Y. Lu, Y. Wu, S. Wang, Y. Zhang, P. Dong, Y. Wang, C. Zhao, S. Wang, J. Zhang, S. Wang, Rejoint of carbon nitride fragments into multi-interfacial disorder-disorder homojunction for robust photo-driven generation of H₂O₂, *Adv. Mater.* (2023) 2307490, <https://doi.org/10.1002/adma.202307490>.

[34] J. Yu, J. González-Cobos, F. Dappozzo, F.J. López-Tenllado, J. Hidalgo-Carrillo, A. Marinas, P. Vernoux, A. Caravaca, C. Guillard, WO₃-based materials for photoelectrocatalytic glycerol upgrading into glyceraldehyde: Unravelling the synergistic photo- and electro-catalytic effects, *Appl. Catal. B* 318 (2022) 121843, <https://doi.org/10.1016/j.apcatb.2022.121843>.

[35] T. Lan, M. Gao, J.-y Hasegawa, Y. Shen, W. Qu, Q. Hu, J. Deng, D. Cheng, D. Zhang, Isolated Pt atoms embedded in CuO nanocatalysts for selective oxidation of ammonia, *ACS Catal.* 13 (2023) 14070–14079, <https://doi.org/10.1021/acscatal.3c02613>.

[36] J. Zheng, S. Impeng, J. Liu, J. Deng, D. Zhang, Mo promoting Ni-based catalysts confined by halloysite nanotubes for dry reforming of methane: insight of coking and H₂S poisoning resistance, *Appl. Catal. B* 342 (2024) 123369, <https://doi.org/10.1016/j.apcatb.2023.123369>.

[37] W. Qu, C. Wang, P. Wang, Y. Shen, J. He, D. Zhang, Insights into reaction pathway induced by d orbital occupancy on cobalt supported boron nitride for N₂O catalytic decomposition, *Appl. Surf. Sci.* 636 (2023) 157792, <https://doi.org/10.1016/j.apsusc.2023.157792>.

[38] W. Qu, P. Wang, M. Gao, J.-y Hasegawa, Z. Shen, Q. Wang, R. Li, D. Zhang, Delocalization effect promoted the indoor air purification via directly unlocking the ring-opening pathway of toluene, *Environ. Sci. Technol.* 54 (2020) 9693–9701, <https://doi.org/10.1021/es.acs.est.0c02906>.

[39] J. Liu, P. Wang, W. Qu, H. Li, L. Shi, D. Zhang, Nanodiamond-decorated ZnO catalysts with enhanced photocorrosion-resistance for photocatalytic degradation of gaseous toluene, *Appl. Catal. B* 257 (2019) 117880, <https://doi.org/10.1016/j.apcatb.2019.117880>.

[40] X. Li, Z. Le, X. Chen, Z. Li, W. Wang, X. Liu, A. Wu, P. Xu, D. Zhang, Graphene oxide enhanced amine-functionalized titanium metal organic framework for visible-light-driven photocatalytic oxidation of gaseous pollutants, *Appl. Catal. B* 236 (2018) 501–508, <https://doi.org/10.1016/j.apcatb.2018.05.052>.

[41] Y. Zhang, M. Wu, Y. Wang, Y.H. Kwok, W. Pan, W. Szeto, H. Huang, D.Y.C. Leung, Fluorinated TiO₂ coupling with α-MnO₂ nanowires supported on different substrates for photocatalytic VOCs abatement under vacuum ultraviolet irradiation, *Appl. Catal. B* 280 (2021) 119388, <https://doi.org/10.1016/j.apcatb.2020.119388>.

[42] J. Li, Z. Huang, C. Wang, L. Tian, X. Yang, R. Zhou, M.N. Ghazzal, Z.-Q. Liu, Linkage effect in the bandgap-broken V₂O₅-GdCr₃ heterojunction by carbon allotropes for boosting photocatalytic H₂ production, *Appl. Catal. B* 340 (2024) 123181, <https://doi.org/10.1016/j.apcatb.2023.123181>.

[43] J. Li, X. Yang, C. Ma, Y. Lei, Z. Cheng, Z. Rui, Selectively recombining the photoinduced charges in bandgap-broken Ag₃Po₄/GdCr₃ with a plasmonic Ag bridge for efficient photothermocatalytic VOCs degradation and CO₂ reduction, *Appl. Catal. B* 291 (2021) 120053, <https://doi.org/10.1016/j.apcatb.2021.120053>.

[44] Y. Zhang, M. Wu, Y.H. Kwok, Y. Wang, W. Zhao, X. Zhao, H. Huang, D.Y.C. Leung, *In-situ* synthesis of heterojunction TiO₂/MnO₂ nanostructure with excellent performance in vacuum ultraviolet photocatalytic oxidation of toluene, *Appl. Catal. B* 259 (2019) 118034, <https://doi.org/10.1016/j.apcatb.2019.118034>.

[45] J. Qin, J. Wang, J. Yang, Y. Hu, M. Fu, D. Ye, Metal organic framework derivative-TiO₂ composite as efficient and durable photocatalyst for the degradation of toluene, *Appl. Catal. B* 267 (2020) 118667, <https://doi.org/10.1016/j.apcatb.2020.118667>.

[46] Xa Dong, W. Cui, H. Wang, J. Li, Y. Sun, H. Wang, Y. Zhang, H. Huang, F. Dong, Promoting ring-opening efficiency for suppressing toxic intermediates during photocatalytic toluene degradation via surface oxygen vacancies, *Sci. Bull.* 64 (2019) 669–678, <https://doi.org/10.1016/j.scib.2019.04.020>.

[47] M. Sun, X. Wang, Z. Chen, M. Muruganathan, Y. Chen, Y. Zhang, Stabilized oxygen vacancies over heterojunction for highly efficient and exceptionally VOCs photocatalytic degradation, *Appl. Catal. B* 273 (2020) 119061, <https://doi.org/10.1016/j.apcatb.2020.119061>.

[48] H. Liu, Y. Ma, J. Chen, M. Wen, G. Li, T. An, Highly efficient visible-light-driven photocatalytic degradation of VOCs by CO₂-assisted synthesized mesoporous carbon confined mixed-phase TiO₂ nanocomposites derived from MOFs, *Appl. Catal. B* 250 (2019) 337–346, <https://doi.org/10.1016/j.apcatb.2019.03.054>.

[49] W. Cui, J. Li, L. Chen, Xa Dong, H. Wang, J. Sheng, Y. Sun, Y. Zhou, F. Dong, Nature-inspired CaCO₃ loading TiO₂ composites for efficient and durable photocatalytic mineralization of gaseous toluene, *Sci. Bull.* 65 (2020) 1626–1634, <https://doi.org/10.1016/j.scib.2020.05.024>.

[50] Hi Kim, H.-n Kim, S. Weon, G.-h Moon, J.-H. Kim, W. Choi, Robust Co-catalytic performance of nanodiamonds loaded on WO₃ for the decomposition of volatile organic compounds under visible light, *ACS Catal.* 6 (2016) 8350–8360, <https://doi.org/10.1021/acscatal.6b02726>.

[51] M. Miyachi, Photocatalysis and photoinduced hydrophilicity of WO₃ thin films with underlying Pt nanoparticles, *Phys. Chem. Chem. Phys.* 10 (2008) 6258, <https://doi.org/10.1039/B807426g>.

[52] Z. Topalian, B.I. Stefanov, C.G. Granqvist, L. Österlund, Adsorption and photo-oxidation of acetaldehyde on TiO₂ and sulfate-modified TiO₂: studies by *in situ* FTIR spectroscopy and micro-kinetic modeling, *J. Catal.* 307 (2013) 265–274, <https://doi.org/10.1016/j.jcat.2013.08.004>.

[53] G. Busca, J. Lamotte, J.C. Lavalle, V. Lorenzelli, FT-IR study of the adsorption and transformation of formaldehyde on oxide surfaces, *J. Am. Chem. Soc.* 109 (1987) 5197–5202, <https://doi.org/10.1021/ja00251a025>.

[54] B. Hauchecorne, D. Terrens, S. Verbruggen, J.A. Martens, H. Van Langenhove, K. Demeester, S. Lenaerts, Elucidating the photocatalytic degradation pathway of acetaldehyde: An FTIR *in situ* study under atmospheric conditions, *Appl. Catal. B* 106 (2011) 630–638, <https://doi.org/10.1016/j.apcatb.2011.06.026>.